



# Biotemplate synthesis of polypyrrole@bacterial cellulose/MXene nanocomposites with synergistically enhanced electrochemical performance

Quancheng Song · Zeying Zhan · Binxia Chen · Zehang Zhou ·  
Canhui Lu

Received: 22 April 2020 / Accepted: 24 June 2020 / Published online: 28 June 2020  
© Springer Nature B.V. 2020

**Abstract** Polypyrrole (PPy) has received extensive attention in supercapacitor electrodes due to its promising electrochemical activity, while the poor cycling stability and densely packed structure limited its electrochemical performance. Herein, we demonstrate the fabrication of flexible and freestanding PPy@bacterial cellulose (BC)/MXene composite film with significantly enhanced electrochemical performance. PPy nanoparticles were uniformly deposited on BC nanofibers via in situ polymerization, and assembled with highly conductive MXene ( $\text{Ti}_3\text{C}_2\text{T}_x$ ) nanoflakes through strong interfacial interactions. BC as a biological template can effectively disperse PPy nanoparticles. The intercalation of PPy@BC nanofibers into  $\text{Ti}_3\text{C}_2\text{T}_x$  layers constructs hierarchically packed nanofibrous structure, which provides

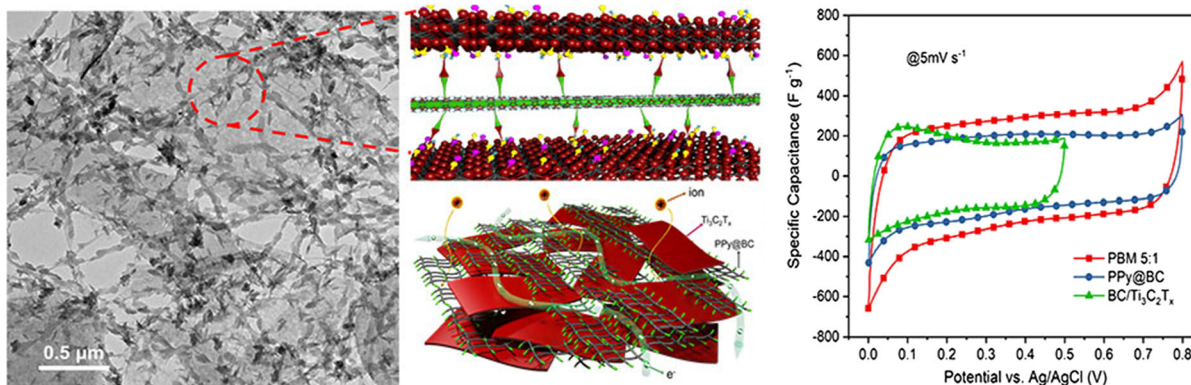
extensive accessible electrochemical active sites. Freestanding PPy@BC/ $\text{Ti}_3\text{C}_2\text{T}_x$  (PBM) electrode exhibits superior specific capacitance (gravimetric and areal capacitance of up to  $550 \text{ F g}^{-1}$  and  $879 \text{ mF cm}^{-2}$ , respectively) and excellent capacitance retention of 83.5% after 10,000 cycles. In addition, the symmetric supercapacitor assembled by PBM papers present a high energy density of  $33.1 \text{ W h kg}^{-1}$  (power density of  $243 \text{ W kg}^{-1}$ ) and excellent capacitance retention. The elaborately designed nanostructure and PPy- $\text{Ti}_3\text{C}_2\text{T}_x$  hybridization make great contribution to the enhanced electrochemical performance, which provide a feasible method for the fabrication of conductive polymer-based high-performance flexible supercapacitor electrodes.

**Electronic supplementary material** The online version of this article (<https://doi.org/10.1007/s10570-020-03310-7>) contains supplementary material, which is available to authorized users.

Q. Song · Z. Zhan · B. Chen · Z. Zhou (✉) · C. Lu (✉)  
State Key Laboratory of Polymer Materials Engineering,  
Polymer Research Institute of Sichuan University,  
Chengdu 610065, People's Republic of China  
e-mail: zzh303@scu.edu.cn

C. Lu  
e-mail: canhuilu@scu.edu.cn

## Graphic abstract



**Keywords** Mxene · Bacterial cellulose · Polypyrrole · Supercapacitor

## Introduction

Rapid widespread of portable electronic devices requires the development of flexible energy storage systems (Simon and Gogotsi 2008). Supercapacitors (SCs) have been widely explored for energy storage application owing to their higher power density, cycle efficiency and rapid charge–discharge rates (Zhang and Zhao 2009; Choi et al. 2012; El-Kady et al. 2016). To date, pseudocapacitive materials such as metal oxides/hydroxides (e.g.,  $\text{RuO}_2$  (Jiang et al. 2018),  $\text{MnO}_2$  (Zhu et al. 2018) and  $\text{Ni}(\text{OH})_2$  (Ke et al. 2017)) or conductive polymers (e.g., polypyrrole (PPy) (Song et al. 2015; Kashani et al. 2016) and polyaniline (Ge et al. 2015)) have been widely used as electrode materials to promote electrochemical performance. Specifically, conductive polymers have become increasingly popular as pseudocapacitive electrode material for SCs in virtue of their low cost, good environmental stability (Wang et al. 2012; Huang et al. 2016; Wan et al. 2017), high conductivity in doped state and high specific capacitance (theoretical of PPy is  $620 \text{ F g}^{-1}$  (Lota et al. 2004)). However, pristine conductive polymers tend to agglomerate during polymerization, which impede the diffusion and transportation of electrolyte ions. Furthermore, conductive polymers suffer from poor cycling

performance owing to the swelling–shrinking behavior during the ion intercalating/deintercalating process.

Recently, transition metal carbides and nitrides, known as MXenes, have arisen as a new family of two-dimensional (2D) functional materials (Lei et al. 2015; Liu et al. 2020; Jin et al. 2020). Among them, titanium carbide ( $\text{Ti}_3\text{C}_2\text{T}_x$ , where  $\text{T}_x$  stands for the surface termination groups) is the most extensively reported material due to its great conductivity (Geng et al. 2019), good hydrophilicity (Ghidiu et al. 2014), and excellent ion intercalation behavior (Lukatskaya et al. 2013; Mu et al. 2019). It has been demonstrated as promising supercapacitor electrode materials with outstanding electrochemical performance (specific capacitance up to  $1500 \text{ F cm}^{-3}$ ) (Anasori et al. 2017; Lukatskaya et al. 2017). Due to its unique advantages,  $\text{Ti}_3\text{C}_2\text{T}_x$  is expected to serve as desirable supporting materials for the conductive polymer-based electrode. Zhi et al. intercalated PPy into the  $\text{Ti}_3\text{C}_2\text{T}_x$  sheet via electrophoretic deposition, which increased the capacitance from 150 to  $203 \text{ mF cm}^{-2}$  (Zhu et al. 2016). Beidaghi et al. reported the oxidant-free polymerization of aniline on the  $\text{Ti}_3\text{C}_2\text{T}_x$  nanoflakes, which intercalated between the  $\text{Ti}_3\text{C}_2\text{T}_x$  layers expanding the interlayer space to facilitate charge transport (VahidMohammadi et al. 2018). Gogotsi et al. prepared hybrid electrodes by in-situ synthesis of pyrrole on  $\text{Ti}_3\text{C}_2\text{T}_x$ , in which the capacitance of the  $13 \mu\text{m}$  thick electrode was as high as  $416 \text{ F g}^{-1}$  (Boota et al. 2016). The incorporation of MXene is a feasible strategy to improve the electrochemical performance of intrinsic conductive polymers.

Herein, we report the fabrication of flexible and freestanding PPy@bacterial cellulose (BC)/Ti<sub>3</sub>C<sub>2</sub>T<sub>x</sub> film (PBM) with well-enhanced electrochemical performance. PBM with hierarchically packed nanofibrous structure was synthesized through BC templated pyrrole polymerization and subsequent self-assembly with Ti<sub>3</sub>C<sub>2</sub>T<sub>x</sub> nanoflakes. Nanocellulose, such as cellulose nanofibrils (CNFs) and bacterial cellulose (BC), has proven to be a promising candidate for green novel energy device due to its excellent mechanical properties, large specific surface area, light weight and flexibility (Du et al. 2017; Wang et al. 2018; Li et al. 2018). For example, Edberg et al. combined cellulose nanofibrils, sulfonated lignin and conductive polymer to produce supercapacitors with excellent rate performance (Edberg et al. 2018); Zhang et al. used wood cellulose as the raw material and manipulated the carbonization temperature to control the nanofiber structure to obtain high-performance supercapacitors (Zhang et al. 2019). Compared with CNFs prepared by physical method and TEMPO-CNFs prepared by chemical method, BC has very high cellulose content (higher than 99%) and can be easily obtained through simple and non-toxic processing steps (Wu et al. 2016). Meanwhile, the crystallinity of BC comprised of 2–4 nm nanofibrils exceeds 70%, resulting in excellent mechanical robustness (Zhao et al. 2020). Based on the green chemistry and recycling economy, these 1D flexible, low-cost and environmentally friendly BC nanofibers with nanofibrous network are appealing substrate, serving not only as template for uniform deposition of PPy nanoparticles, but the resulted PPy@BC nanofibers intercalated into Ti<sub>3</sub>C<sub>2</sub>T<sub>x</sub> layers can also effectively prevented restacking of Ti<sub>3</sub>C<sub>2</sub>T<sub>x</sub> and expand their interlayer space. Moreover, the Ti<sub>3</sub>C<sub>2</sub>T<sub>x</sub> nanoflakes were closely contacted with PPy@BC hybrid nanofibers to construct continuous conductive pathways. The synergistic enhancement effect endows PBM with good flexibility, high conductivity and facilitates charges/ions diffusion, which greatly contributed to the improved capacitance and cyclic stability. This work provides a simple and feasible strategy to design and fabricate MXene/conductive polymer-based SCs electrode with enhanced electrochemical performance.

## Experimental section

### Materials

All starting materials and reagents were obtained from commercial sources and used without further purification unless otherwise noted. BC aqueous dispersion was purchased from Qihong Co., Ltd, Guilin, China. Ferric chloride hexahydrate (FeCl<sub>3</sub>·6H<sub>2</sub>O, AR) was purchased from Kermel Chemical Reagent Co., Ltd. Lithium fluoride (LiF, AR) and Pyrrole (Py, AR) was purchased from Aladdin Inc. (China). Ti<sub>3</sub>AlC<sub>2</sub> powder (400 mesh) was purchased from 11 Technology Co., Ltd. (China).

### Preparation of delaminated MXene (Ti<sub>3</sub>C<sub>2</sub>T<sub>x</sub>) nanoflakes

Ti<sub>3</sub>C<sub>2</sub>T<sub>x</sub> was prepared by selectively etching off aluminum atoms in MAX powder. In a typical experiment, Ti<sub>3</sub>AlC<sub>2</sub> powder was added to a 9 M hydrochloric acid solution (HCl) in which LiF salt was dissolved (Ti<sub>3</sub>AlC<sub>2</sub>:LiF = 1:1 wt./wt.). The etching solution was continuously stirred at 35 °C for 36 h. Subsequently, the etched Ti<sub>3</sub>C<sub>2</sub>T<sub>x</sub> solid residue was washed with deionized water and centrifuged at 3500 rpm until the supernatant pH exceed 6. Then the sediment was re-dispersed in deionized water by hand-shaking, followed by centrifugation at 3500 rpm for 5 min to obtain the Ti<sub>3</sub>C<sub>2</sub>T<sub>x</sub> nanoflakes aqueous dispersion. The concentration of the Ti<sub>3</sub>C<sub>2</sub>T<sub>x</sub> solution was determined by vacuum filtration of a known weight of the supernatant into a film.

### Preparation of PPy@BC conductive nanocomposites

The PPy@BC conductive nanocomposites are prepared by in-situ oxidative polymerization of pyrrole self-assembled onto BC. A typical synthesis was as follows. Freshly prepared BC aqueous dispersion (50 g, 0.2 wt%) was added to dimethyl formamide (DMF) solution (2:1, v/v) and stirred vigorously to fully disperse BC nanofibers at 25 °C. Pyrrole (6 mmol, 1 g) was added to the BC suspension and stirred vigorously for 0.5 h to fully self-assemble onto the surface of the BC nanofibers. Then, a mixed solution of ferric chloride hexahydrate (FeCl<sub>3</sub>·6H<sub>2</sub>O, 7 mmol, 1.89 g) and 1 M HCl (18 mmol) were added,

in which  $\text{FeCl}_3 \cdot 6\text{H}_2\text{O}$  was used as oxidant catalyst and HCl was used as dopant. The reaction temperature was controlled at 0–4 °C and the reaction time is 6–8 h. After reaction was completed, the resulting precipitate was sequentially washed with ethanol, deionized water and 1 M HCl to remove monomers and oxidants. Finally, the washed product was re-dissolved in 1 M HCl to make PPy@BC black suspension, and the PPy@BC concentration was determined by measuring the residual mass after drying a certain mass of the suspension. For reference, pristine PPy was also synthesized by oxidation polymerization of pyrrole with  $\text{FeCl}_3 \cdot 6\text{H}_2\text{O}$  (7 mmol, 1.89 g) as oxidant and 1 M HCl (18 mmol) as dopant in  $\text{H}_2\text{O}$ -DMF (2:1, v/v) at 4 °C.

### Preparation of PBM conductive paper

Delaminated  $\text{Ti}_3\text{C}_2\text{T}_x$  nanoflakes and PPy@BC nanofibers were respectively dispersed in deionized water with a concentration of 0.2 wt% and 0.1 wt%. Different amount of  $\text{Ti}_3\text{C}_2\text{T}_x$  dispersion was added into the PPy@BC dispersion with stirring. The mixture of  $\text{Ti}_3\text{C}_2\text{T}_x$  and PPy@BC was continuously stirred for 4 h. Then the suspension was filtered through vacuum-assisted filtration to obtain PBM composite paper. The mass ratio of PPy@BC to  $\text{Ti}_3\text{C}_2\text{T}_x$  in the composite film were 7:1, 5:1, 3:1, 1:1, 1:3 and 1:5, which were denoted as PBM 7:1, 5:1, 3:1, 1:1, 1:3 and 1:5, respectively. Depending on the proportion of PPy@BC and  $\text{Ti}_3\text{C}_2\text{T}_x$ , the thickness of the prepared PBM conductive films were between 45  $\mu\text{m}$  and 67  $\mu\text{m}$  (details are shown in Table S1). PPy@BC and BC/ $\text{Ti}_3\text{C}_2\text{T}_x$  papers were also fabricated under the same conditions for comparison.

### Characterizations and electrochemical measurements

The morphology and microstructure of BC, PPy@BC, BC/ $\text{Ti}_3\text{C}_2\text{T}_x$  and PBM composite paper were studied by scanning electron microscopy (SEM) on a microscope (JSM-5600, JEOL, Japan). Transmission electron microscopy (TEM) was performed using a transmission electron microscope (JEOL JEM-100CX, Japan) to intuitively observe the morphology of  $\text{Ti}_3\text{C}_2\text{T}_x$  nanoflakes, BC nanofibers, PPy@BC nanofibers and PBM composite. A Nicolet 6700 spectrophotometer (USA) with attenuated total

reflectance (ATR) mode was used to collect Fourier transform infrared spectroscopy (FTIR) at ambient temperature. X-ray diffraction (XRD) patterns of  $\text{Ti}_3\text{C}_2\text{T}_x$  film, BC film, PPy@BC film and PBM composite film were recorded with a Philip X pert PRO MPD (Philips Co., Netherlands) X-ray diffractometer. Cu  $K\alpha$  radiation ( $\lambda = 1.54 \text{ \AA}$ ) at a generator current of 50 mA was used as the radiation source and the generator voltage was set as 40 kV with a scanning speed of 4°/min. Tensile tests of samples were measured using a universal tensile testing machine (Instron-5560, USA) with an extension rate of 100 mm/min at room temperature. The electric resistance of all samples was measured by a four-point probe measurement with an M-3 mini type four-probe tester (Suzhou Jingge Electronic Co., Ltd., China).

VersaSTAT3 electrochemical workstation was employed to measure the electrochemical performance of the as-prepared electrodes. A plastic Swagelok cells was used to perform the electrochemical tests. The fabricated freestanding films, over capacitive activated carbon, and Ag/AgCl served as the working electrode, counter electrode, and reference electrode, respectively. A glassy carbon electrode was used as current collectors for the working electrodes. The electrochemical impedance spectroscopy (EIS) was conducted within a frequency range from 200 kHz to 0.01 Hz at an amplitude of 10 mV.

## Results and discussion

### Morphologies and structures

Figure 1 shows the strategy for the preparation of flexible and freestanding PBM composite film. The PPy@BC nanofibers were fabricated by in situ oxidative polymerization of pyrrole with BC as the biotemplate (Fig. 1a). A mixture of ferric chloride hexahydrate ( $\text{FeCl}_3 \cdot 6\text{H}_2\text{O}$ ) and hydrochloric acid (HCl) were added into the BC/pyrrole suspension as oxidant catalyst and dopant, respectively. Pyrrole monomers were deposited on the surface of BC through hydrogen bonding between pyrrole ring and BC. As reaction proceeded, the BC/pyrrole suspension was observed to change from semi-translucent ivory dispersion to suspended dark agglomerates, demonstrating that the surface of BC nanofibers was

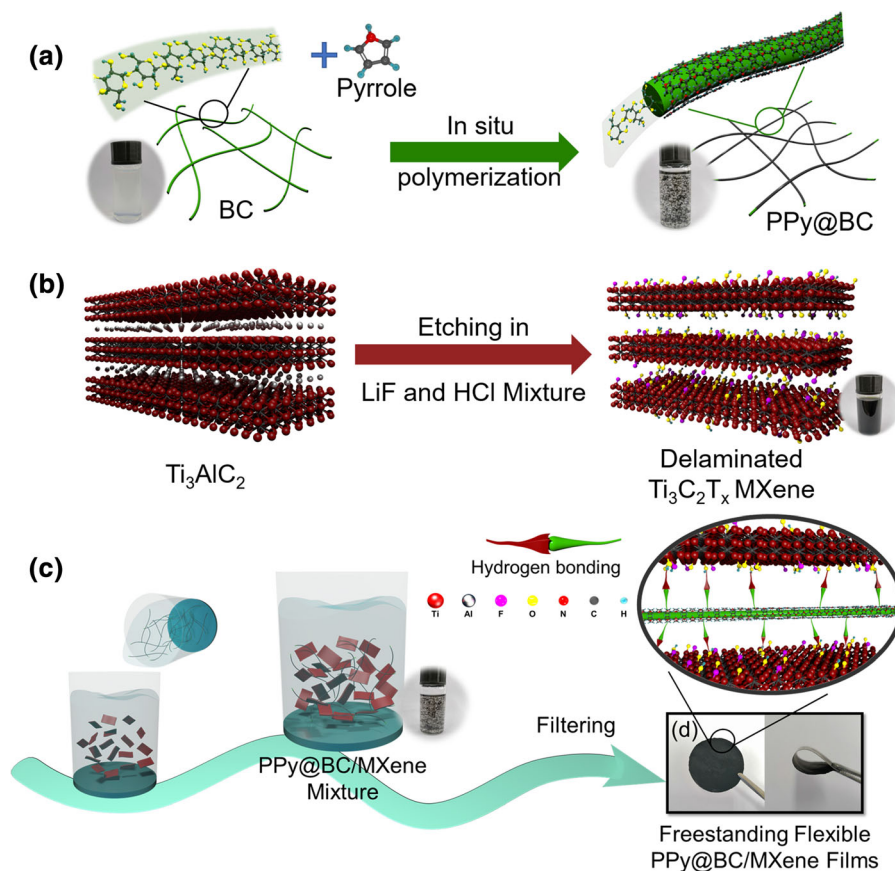


**Fig. 1** Schematic illustration of the synthesis of PBM composite paper. **a** Schematic illustration of the synthesis of PPy@BC by in situ oxidative polymerization of pyrrole with BC as the template. **b** Schematic diagram of  $Ti_3C_2T_x$  obtained by selective etching of aluminum atomic layer from layered

$Ti_3AlC_2$  phase. **c** Illustration and photograph of PPy@BC and  $Ti_3C_2T_x$  mixture. PPy@BC nanofibers rely on hydrogen bonding to make close contact with  $Ti_3C_2T_x$  nanoflakes. **d** Image of the freestanding PBM paper and demonstration of the flexibility of the freestanding PBM film

uniformly coated with the obtained PPy, which blocked their hydrophilic hydroxyl groups. Figure 1b schematically shows the synthesis process of  $Ti_3C_2T_x$ . The delaminated  $Ti_3C_2T_x$  dispersion was prepared by eliminating Al atomic layer in the  $Ti_3AlC_2$  (MAX) phase structure through etching by LiF and HCl mixed solution and subsequent hand shaking delamination. TEM image (Fig. S1) shows that the delaminated  $Ti_3C_2T_x$  nanoflakes present flat and almost transparent lamellar morphology with average transverse size of several hundred nanometers. The delaminated  $Ti_3C_2T_x$  nanoflakes can form stable and uniform dispersion in aqueous solution. Then PPy@BC and  $Ti_3C_2T_x$  dispersions were mixed to obtain PBM dispersions (Fig. 1c), and freestanding flexible PBM films were obtained through vacuum-assisted filtration (Fig. 1d). The  $Ti_3C_2T_x$  nanoflakes closely contacted with

PPy@BC nanofibers through hydrogen bonding. As a result, the PBM suspension exhibits black suspended agglomerates similar to the PPy@BC suspension.

Figure 2a and d exhibit scanning electron microscope (SEM) and transmission electron microscope (TEM) images of pristine BC. BC nanofibers with a diameter between 10 and 40 nm exhibit smooth surface and nanofibrous network, which is similar to the morphology of previously reported BC nanofibers (Qiu et al. 2016). Their 1D structure and high aspect ratio makes an excellent template for loading active materials. Meanwhile, the existence of hydrogen bonding that acts as traction force between pyrrole monomer and BC hydroxyl group is a necessary guarantee for the uniform deposition of PPy on the BC surface (Ma et al. 2016a). After in situ polymerization, PPy nanoparticles with a diameter of 50–60 nm were

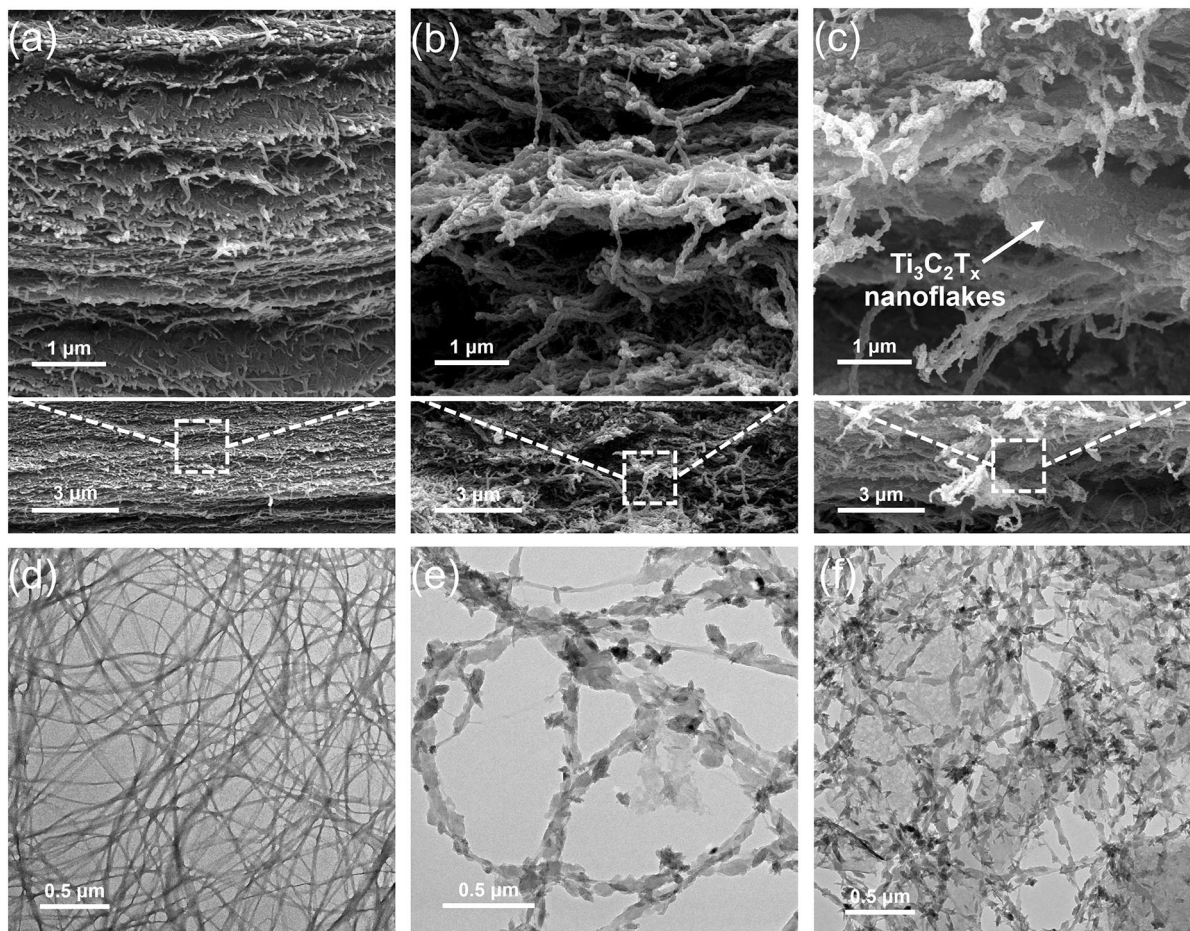


**Fig. 2** SEM images of **a** Pristine BC film, **b** PPy@BC film and **c** PBM composite film. TEM images of **d** Pristine BC dispersion, **e** PPy@BC aqueous dispersion and **f** PBM aqueous dispersion

uniformly grown on the surface of BC nanofibers to form string-bead-like structure (Fig. 2b, e), and the interconnected nanofibrous structure of BC was well-reserved after polymerization (the mass ratio of PPy and BC nanofibers in the synthesized PPy@BC is 7:1). SEM of the PBM (Fig. 2c) presents that  $\text{Ti}_3\text{C}_2\text{T}_x$  nanoflakes are embedded in interconnected PPy@BC nanofibers network without regional agglomeration. The uniform distribution of  $\text{Ti}_3\text{C}_2\text{T}_x$  in PBM is further demonstrated by elemental mapping images (Fig. S2). The nanofibrous structure in composite film is expected to provide accessible active sites and ion diffusion channels. As shown in Fig. 2f, intercalation of PPy@BC nanofibers into  $\text{Ti}_3\text{C}_2\text{T}_x$  nanoflakes to form intimate contact and prevent restacking, which are attributed to the hydrogen bonding forces between N–H and hydroxyl groups on PPy@BC and the

oxygen containing groups on the surface of  $\text{Ti}_3\text{C}_2\text{T}_x$ . Their close contact and uniform distribution of  $\text{Ti}_3\text{C}_2\text{T}_x$  nanoflakes facilitate the construction of continuous conductive pathway. The addition of  $\text{Ti}_3\text{C}_2\text{T}_x$  greatly improved electrical conductivity of the composite films (Fig. S3). The conductivity of PPy@BC is only  $136 \text{ S m}^{-1}$ , while it significantly increased to  $14,245 \text{ S m}^{-1}$  when the mass ratio of PPy@BC to  $\text{Ti}_3\text{C}_2\text{T}_x$  is 1:5 (PBM 1:5).

For comparison, PPy/ $\text{Ti}_3\text{C}_2\text{T}_x$  suspension was prepared by directly mixing  $\text{Ti}_3\text{C}_2\text{T}_x$  with PPy nanoparticles dispersion (Fig. S4). The SEM image of PPy/ $\text{Ti}_3\text{C}_2\text{T}_x$  hybrid paper (Fig. S4a) clearly exhibits that large particles of PPy are distributed on  $\text{Ti}_3\text{C}_2\text{T}_x$ , forming severe dense packing. The simple mixed PPy/ $\text{Ti}_3\text{C}_2\text{T}_x$  dispersion is unable to form a complete film via natural drying or filtration as shown in Fig. S4b,

indicating poor processability. In sharp contrast to PPy/Ti<sub>3</sub>C<sub>2</sub>T<sub>x</sub>, the PBM composite films are highly flexible, bendable (Fig. 1d) and present appropriate mechanical strength (Fig. S5), indicating that the introduction of BC not only effectively regulates the morphological structure of PPy to facilitate dispersion, but also greatly improves the processability of nanocomposites.

### FTIR spectroscopy and XRD analysis

PBM hybrid films were further characterized by Fourier transform infrared (FT-IR) spectroscopy and X-ray diffraction (XRD). As shown in Fig. 3a, pristine PPy exhibits a band at 1644 cm<sup>-1</sup> due to the N–H in plane bending vibration, band at 1540 cm<sup>-1</sup> corresponding to the C = C stretching vibration in the pyrrole ring, broad band at 1440 cm<sup>-1</sup> attributed to the C–N stretching vibration, and band at 1160, 1045 cm<sup>-1</sup> related to C–H in-plane ring stretching vibration (Liu et al. 2015; Ma et al. 2016a). For PPy@BC, the C–O stretching vibration peaks of BC

(1157, 1049 cm<sup>-1</sup>) are redshifted to 1118, 1018 cm<sup>-1</sup> respectively, indicating the hydrogen bonding between BC and PPy. The obvious peaks at 1648, 1533, 1437 and 1284 cm<sup>-1</sup> are attributed to the N–H in plane bending vibration, C=C, C–N ring-stretching vibration and C–N in-plane deformation modes of PPy respectively (Wang et al. 2013; Xu et al. 2013), which demonstrates that BC nanofibers are wrapped with PPy. While for PBM composite film, the peaks belonging to PPy@BC are still retained (1645, 1533, 1435, 1284, 1120 and 1018 cm<sup>-1</sup>), but the characteristic peak of N–H wagging shifts from 862 to 840 cm<sup>-1</sup> and became wider and stronger, indicating the formation of hydrogen bonding between Ti<sub>3</sub>C<sub>2</sub>T<sub>x</sub> and PPy.

XRD patterns were shown in Fig. 3b, the pattern of pristine BC displays three sharp peaks at 14.6°, 16.8° and 22.7°, corresponding to the typical (1  $\bar{1}$  0), (1 1 0) and (2 0 0) diffraction planes of cellulose I, respectively (Ma et al. 2016b). Pure PPy is known to be amorphous and has a broad diffraction peak at  $\approx$  25°, corresponding to the scattering of PPy chains (He et al.

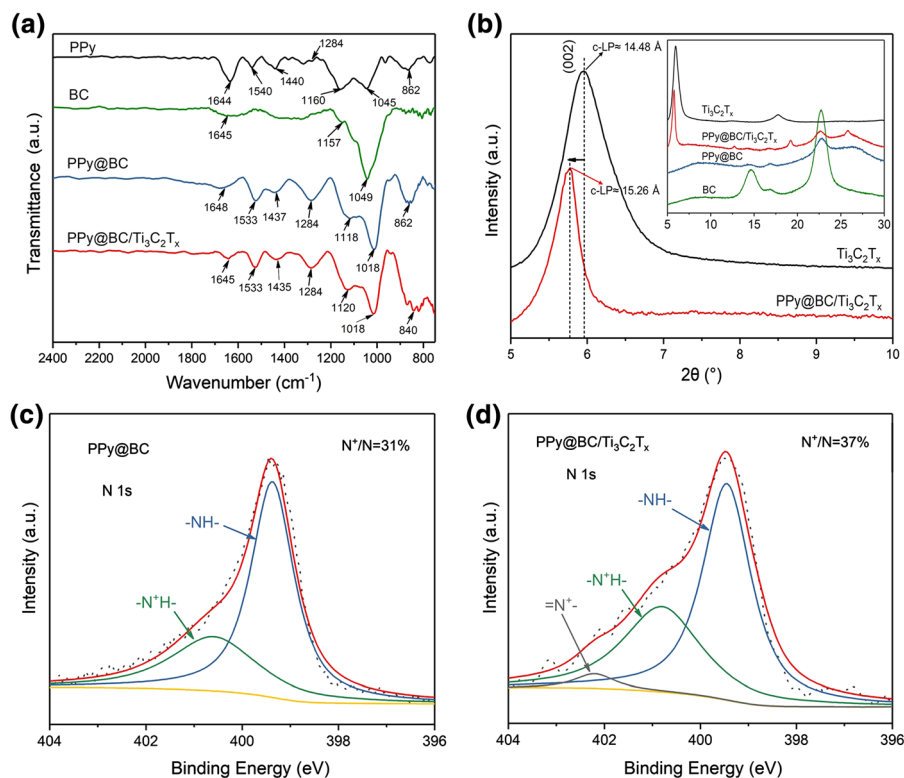


**Fig. 3** **a** FTIR spectrum of pristine PPy, pristine BC, PPy@BC, and PPy@BC/Ti<sub>3</sub>C<sub>2</sub>T<sub>x</sub>. **b** XRD patterns of Ti<sub>3</sub>C<sub>2</sub>T<sub>x</sub>, pristine BC, PPy@BC, and PPy@BC/Ti<sub>3</sub>C<sub>2</sub>T<sub>x</sub>. XPS spectra of the N1s core level of the **c** PPy@BC and **d** PPy@BC/Ti<sub>3</sub>C<sub>2</sub>T<sub>x</sub>

2019). After polymerization of PPy onto the BC, the pattern of PPy@BC exhibits significantly weakened characteristic peaks of BC and PPy. While in the XRD pattern of PBM, the characteristic peaks of BC and PPy are retained, and a new sharp strong peak appears near  $6^\circ$  attributing to the incorporation of  $\text{Ti}_3\text{C}_2\text{T}_x$  (Naguib et al. 2014). The downshift from  $\approx 5.96^\circ$  to  $5.78^\circ$  in the  $\text{Ti}_3\text{C}_2\text{T}_x$  (002) peak of PBM indicates an increased interlayer spacing between  $\text{Ti}_3\text{C}_2\text{T}_x$  layers, which is attributed to the intercalation of PPy@BC nanofibers (Cao et al. 2018).

### XPS spectroscopy

To further explore the interaction between PPy and  $\text{Ti}_3\text{C}_2\text{T}_x$ , the chemical state of N in the PPy backbone was revealed by X-ray photoelectron spectroscopy (XPS). Figure 3c shows the N1s spectra of PPy@BC. The core N1s spectrum has been deconvoluted into neutral nitrogen ( $-\text{NH}-$ ) at 399.7 eV and protonation benzenoid amine ( $-\text{N}^+\text{H}-$ ) at 400.8 eV (Ge et al. 1994). After addition of  $\text{Ti}_3\text{C}_2\text{T}_x$ , a new Gaussian peak appeared at high energy tail (Fig. 3d), corresponding to the protonation quinonoid imine ( $-\text{N}^+=$ ). The polaron ratio ( $\text{N}^+/\text{N}$ ), defined as the area ratio between polaron peak ( $-\text{N}^+\text{H}-$  and  $-\text{N}^+=$ ) and the total nitrogen peak ( $-\text{NH}-$ ,  $-\text{N}^+\text{H}-$  and  $-\text{N}^+=$ ), increased from 31 to 37%. This may be attributed to the coactions between PPy and  $\text{Ti}_3\text{C}_2\text{T}_x$ , such as hydrogen bonding between the  $-\text{OH}$  groups of  $\text{Ti}_3\text{C}_2\text{T}_x$  flakes and the nitrogen lone pairs of PPy. Polarons are generally considered to provide electrochemical activity (Song et al. 2014). The increase in the polaron indicates that there may be more ions and electrons to contribute to increase the electrochemical activity.

### Electrochemical performances of PBM films in three-electrode system

The electrochemical performances of the fabricated freestanding films were evaluated in a three-electrode system with Ag/AgCl electrode as reference electrode. 3 M  $\text{H}_2\text{SO}_4$  was used as electrolyte due to its high conductivity, which facilitates the surface redox reactions of PPy (Boota et al. 2015). Figure 4a compares the CV curves of PBM films with different PPy and  $\text{Ti}_3\text{C}_2\text{T}_x$  contents, all of which are quasi-rectangle, indicating excellent electrochemical reversibility. As PPy content increases, the area of

the curve gradually increases. PBM 5:1 exhibits highest capacitance ( $550 \text{ F g}^{-1}$ ,  $879 \text{ mF cm}^{-2}$ , the active material loading is  $3.21 \text{ mg cm}^{-2}$ ), which is among the best values of previous reported similar electrode materials (Table S2). This may be attributed to the uniform regulation of morphology of PPy nanoparticles via BC biotemplate polymerization and the intercalation of nanofibers into  $\text{Ti}_3\text{C}_2\text{T}_x$  layers, resulting in more accessible active sites and high electrochemical activity. PBM 5:1 in the GCD curve (Fig. 4b) has longest discharge time, typical quasi-triangular shape and low IR drop, indicating optimized charge transfer and charge storage capability. Figure 4c intuitively compares the gravimetric capacitance and area capacitance of different PBM films. The capacitance of PBM 5:1 is 8.2% and 38.7% higher than that of PBM 3:1 ( $505 \text{ F g}^{-1}$ , the active material loading is  $2.80 \text{ mg cm}^{-2}$ ) and PBM 7:1 ( $337 \text{ F g}^{-1}$ , the active material loading is  $2.27 \text{ mg cm}^{-2}$ ), respectively. The possible reason is that the optimum loading of  $\text{Ti}_3\text{C}_2\text{T}_x$  in PBM composite reached a good balance between high charge density and Faraday capacitance provided by p-type doped PPy and excellent electrical conductivity resulted from  $\text{Ti}_3\text{C}_2\text{T}_x$  (Snook et al. 2011; Xiong et al. 2018). It is worth noting that  $\text{Ti}_3\text{C}_2\text{T}_x$  exhibits higher redox capacitance at negative potentials (Boota and Gogotsi 2019), so the PBM 1:1 (the active material loading is  $3.32 \text{ mg cm}^{-2}$ ) hybrid electrode with more  $\text{Ti}_3\text{C}_2\text{T}_x$  has the lowest capacitance in our voltage window. Therefore, PBM 5:1 was chosen for the comparative study of electrochemical performance (Other PBM films are shown in Fig. S6). The CV curve (Fig. 4d) exhibits a typical EDLC rectangular shape below  $100 \text{ mV s}^{-1}$ , indicating good capacitive behavior. As scan rate increases, the rectangular shape of CV curve gradually deviated, which may be caused by the polarization of electrode and increase of the overpotential of ion transport between electrolyte and electrode material (Zhang et al. 2014). The quasi-triangular galvanostatic charging-discharging curves (GCD) at different current densities of 1, 2, 4, 6, 8 and  $10 \text{ mA cm}^{-2}$  (Fig. 4e) further demonstrate the high reversibility of charging-discharging process.

Electrochemical impedance spectroscopy (EIS) measurements were performed to understand the kinetics of electrode process. Nyquist plots (Fig. 4f) of PBM films include two regions, high frequency region of semi-circular arc and low frequency region



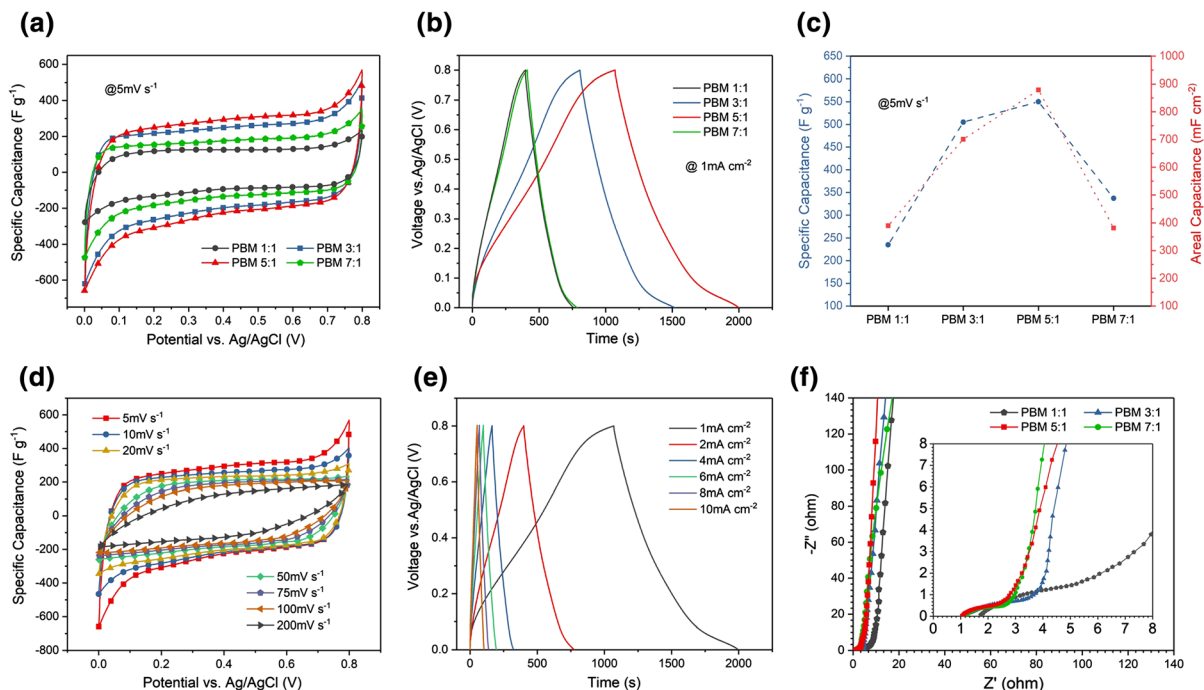


**Fig. 4** Characterization of electrochemical properties of PBM composites: **a** Comparison of cyclic voltammograms (CV) curves of PBM 1:1 3:1 5:1 and 7:1 at scan rate of  $5 \text{ mV s}^{-1}$ . **b** Galvanostatic charge–discharge (GCD) curves of PBM 1:1 3:1 5:1 and 7:1 at  $1 \text{ mA cm}^{-2}$ . **c** Effect of different PPy@BC and  $\text{Ti}_3\text{C}_2\text{T}_x$  contents on gravimetric capacitance and areal

capacitance measured at  $5 \text{ mV s}^{-1}$ . The dotted line between the points is for visual viewing. **d** CV curves of PBM 5:1 film at various scan rates. **e** GCD curves of PBM 5:1 film at various current densities. **f** Nyquist impedance plots of PBM 1:1 3:1 5:1 and 7:1. The inset magnifies the high-frequency region

of straight line, respectively. All curves have similar approximate vertical lines in the low frequency region, indicating rapid diffusion of ions between electrolyte solution and electrode interface. The diameter of semi-circular arc in the high frequency region is usually related to charge transfer resistance. And the smallest semicircle of PBM 5:1 indicates that the proper addition of  $\text{Ti}_3\text{C}_2\text{T}_x$  greatly enhances electrical conductivity of flexible film. As a result, PBM 5:1 presents well-balanced conductivity and charge density, which leads to improved capacitance. Further studies were conducted on sample PBM 5:1.

Comparative study of PBM with PPy@BC and BC/ $\text{Ti}_3\text{C}_2\text{T}_x$  composite electrode films were conducted to further elucidate the electrochemical properties of PBM as shown in Fig. 5. The CV curve of BC/ $\text{Ti}_3\text{C}_2\text{T}_x$  has a quasi-rectangular shape in the potential range of 0–0.5 V (Fig. 5a), while the introduction of PPy leads to extended potential range (from 0 to 0.8 V) and significantly improved gravimetric capacitance ( $550 \text{ F g}^{-1}$  for PBM 5:1, 53.6% higher than that of

BC/ $\text{Ti}_3\text{C}_2\text{T}_x$   $255 \text{ F g}^{-1}$  and the active material loading of BC/ $\text{Ti}_3\text{C}_2\text{T}_x$  is  $8.16 \text{ mg cm}^{-2}$ ). PPy uniformly deposited on the surface of BC nanofibers provides extensive accessible active sites and excellent electrochemical activity, which significantly improve the capacitance. Furthermore, the specific capacitance of PBM 5:1 is 30.9% higher than PPy@BC ( $380 \text{ F g}^{-1}$ , the active material loading is  $2.68 \text{ mg cm}^{-2}$ ), and the areal capacitance of PBM 5:1 ( $879 \text{ mF cm}^{-2}$ ) is 42.1% higher than PPy@BC ( $509 \text{ mF cm}^{-2}$ ). The improved capacitance is attributed to the uniform distribution of  $\text{Ti}_3\text{C}_2\text{T}_x$  nanoflakes incorporated on the surface of nanofibers, which constructed continuous conductive pathways and increased long-range transport channels of electrons and ions (schematic illustration displayed in Fig. 5f). The GCD curves of PBM 5:1, PPy@BC and BC/ $\text{Ti}_3\text{C}_2\text{T}_x$  films (Fig. 5b) present approximate triangle shapes, indicating high reversibility of redox reactions and good coulombic efficiency. PBM 5:1 has the longest discharge time, indicating its highest capacitance. The

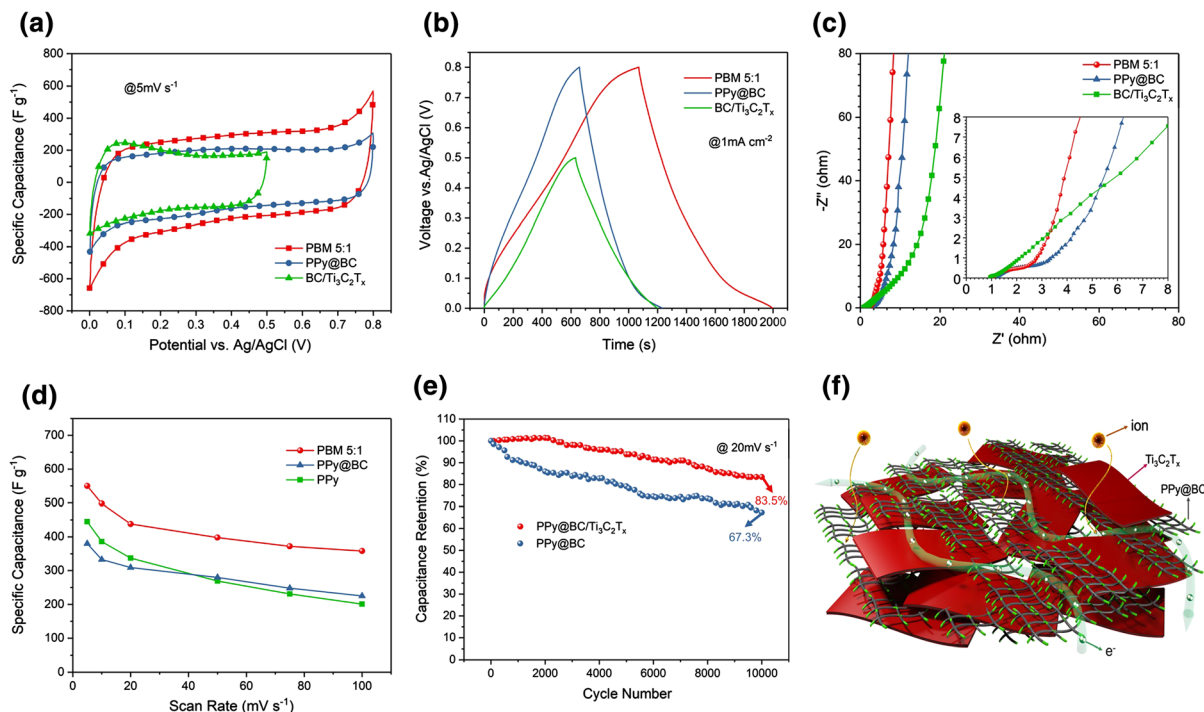


**Fig. 5** Comparison of electrochemical performance: **a** Cyclic voltammograms (CV) at  $5 \text{ mV s}^{-1}$ . **b** Galvanostatic charge–discharge cycles (GCD) at current densities of  $1 \text{ mA cm}^{-2}$ . **c** Nyquist plots. The inset magnifies the high-frequency region. **d** Gravimetric capacitance of PBM 5:1, PPy@BC and pristine

electrochemical performance of pristine PPy, PPy@BC, and BC/Ti<sub>3</sub>C<sub>2</sub>T<sub>x</sub> composites are shown in Fig. S7. Figure 5c compares the Nyquist plots of PBM 5:1, PPy@BC and BC/Ti<sub>3</sub>C<sub>2</sub>T<sub>x</sub>. The low real-axis intercept value for each sample indicates low series resistance, which makes them attractive for supercapacitor electrodes. The plot of PBM 5:1 is almost vertical in the low frequency region, indicating its excellent capacitive behavior. For comparison, the straight line of BC/Ti<sub>3</sub>C<sub>2</sub>T<sub>x</sub> is inclined, corresponding to high ion diffusion impedance. In high frequency region, the width of semi-circular arc of PBM 5:1 is between PPy@BC and BC/Ti<sub>3</sub>C<sub>2</sub>T<sub>x</sub>, which demonstrates that the addition of Ti<sub>3</sub>C<sub>2</sub>T<sub>x</sub> effectively reduces charge transfer resistance.

Figure 5d compares rate-dependent behavior of PBM 5:1, PPy@BC, and pristine PPy. The dense packing structure of PPy leads to reduced active site and hinders in-time ions intercalation/extraction, resulting in capacitance retention of 45% at  $100 \text{ mV s}^{-1}$ . However, the capacitance retention rates

of PPy versus different scan rate. **e** Cycling stability of PBM 5:1 and PPy@BC electrode measured at  $20 \text{ mV s}^{-1}$ , confirming the high cycle stability of PPy in the PBM composite. **f** Schematic illustration of ions and electrons transport in PBM electrode

of PPy@BC and PBM 5:1 at  $100 \text{ mV s}^{-1}$  are 59% and 65%, respectively. This is attributed to the fact that BC template effectively regulates the aggregation mode of PPy resulting in uniform dispersion and high conductivity of Ti<sub>3</sub>C<sub>2</sub>T<sub>x</sub>. Figure 5e shows cycling stability of PBM 5:1 and PPy@BC. Generally, pristine PPy exhibits poor cycling stability due to structural polarization and counterion drain effect (Heinze et al. 2010; Liu et al. 2014). The capacitance retention of PPy@BC drops to 67.3% after 10,000 cycles at  $20 \text{ mV s}^{-1}$ . To contrast, the capacitance retention of PBM 5:1 is as high as 83.5%. The well-improved capacitance retention during cycling may be attributed to close contact between PPy@BC and Ti<sub>3</sub>C<sub>2</sub>T<sub>x</sub> nanoflakes which effectively inhibit swelling-shrinking during ion intercalating and deintercalating process.

## Symmetric supercapacitor

In order to further evaluate the capacitor devices performance of freestanding PBM composite papers, electrochemical characterization was performed by sandwiching two PBM 5:1 films into a symmetric supercapacitor (Fig. 6). The CV curves (Fig. 6a and S8) appear distortion because scan rate increases from 1 to 100  $\text{mV s}^{-1}$  resulting in potential polarization of the PBM electrode. The GCD curves at different current densities (Fig. 6b) present quasi-triangle shapes, revealing low resistance, fast ion and electron transfer kinetics and high coulombic efficiency (Boota and Gogotsi 2019). Gravimetric capacitance of PBM symmetric supercapacitor was calculated from discharge curve of GCD (Fig. 6c). The capacitance at current density of 1  $\text{mA cm}^{-2}$  is 294  $\text{F g}^{-1}$ . As the current of charging and discharging process gradually increases, PBM electrode exhibits great capacitance retention. The capacitance is 236  $\text{F g}^{-1}$  when current

density is increased to 10  $\text{mA cm}^{-2}$ , which is only 19.7% lower than the value of 1  $\text{mA cm}^{-2}$ . In addition, the energy density of up to 33.1  $\text{Wh kg}^{-1}$  (power density of 243  $\text{W kg}^{-1}$ ) can be obtained with specific capacitance at 1  $\text{mA cm}^{-2}$ , surpassing most previous reported similar symmetric supercapacitor (Fig. 6d and detailed comparison data is given in Table S3). High capacitance, excellent energy density and outstanding capacitance retention of PBM symmetric supercapacitors can be attributed to the well-designed PBM nanostructures and synergies between components. EIS curve (Fig. 6e) shows a small semi-circular arc in the high frequency region and a nearly vertical straight line in the low frequency region, which also reveal that the device has low transfer resistance and fast ion electron transport. Additionally, three PBM symmetric supercapacitors were assembled in series into one energy storage device. After charging to 3 V, it is demonstrated that a red LED light can be easily illuminated (Fig. 6f).

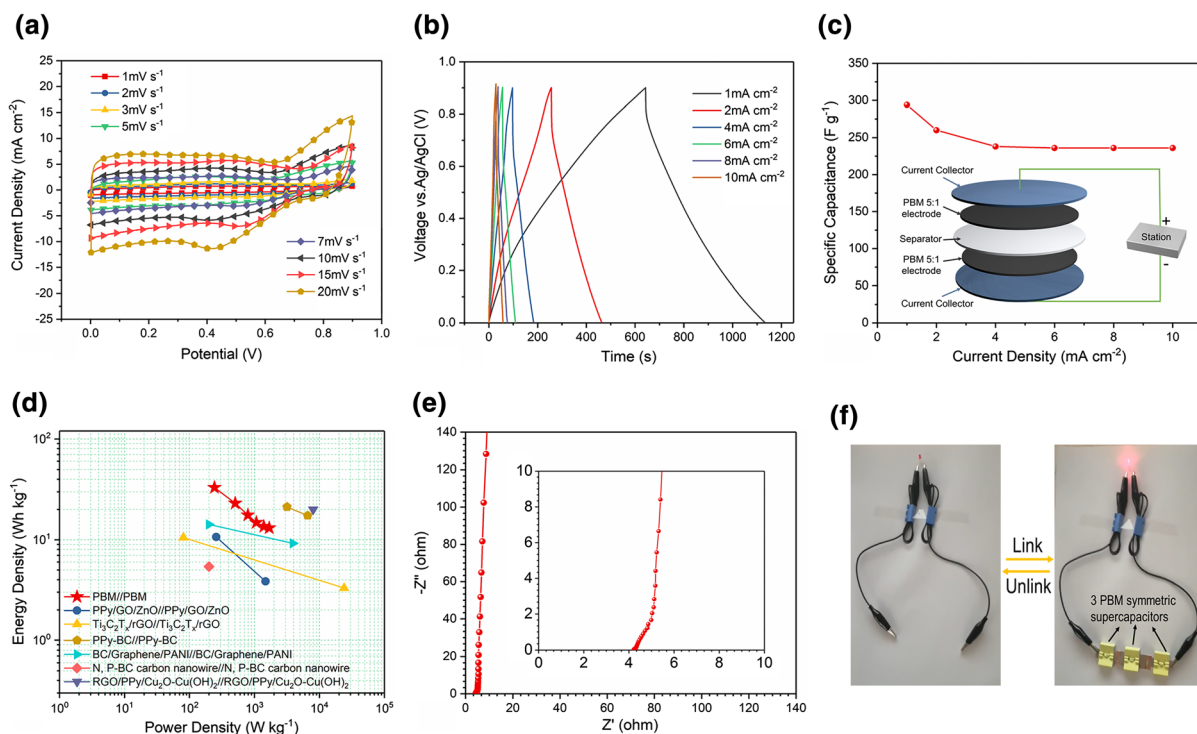


**Fig. 6** Electrochemical performance of PBM symmetric supercapacitors: **a** Cyclic voltammetry curves of PBM symmetric supercapacitors at different scan rate. **b** Galvanostatic charge–discharge curves at various current densities. **c** Gravimetric capacitance under different current densities. The illustration shows the structure of PBM symmetrical two-

electrode supercapacitor. **d** Ragone plots of PBM symmetric supercapacitor in comparison to other PPy-based symmetric supercapacitors. **e** Nyquist plots. The inset magnifies the high-frequency region. **f** Three PBM symmetric supercapacitors in series illuminate a red LED light

## Conclusions

In summary, we demonstrate a facile strategy for the fabrication of PPy@BC/Ti<sub>3</sub>C<sub>2</sub>T<sub>x</sub> composite film through in situ polymerization of PPy on BC nanofibers and their self-assembly with Ti<sub>3</sub>C<sub>2</sub>T<sub>x</sub> nanoflakes. As a template, BC effectively regulates the morphology of PPy nanoparticles to prevent dense packing, and intimately contacts Ti<sub>3</sub>C<sub>2</sub>T<sub>x</sub> nanoflakes through hydrogen bonding, resulting a hierarchically packed nanofibrous structure and conductive pathways. The elaborately designed structure and the synergistic effect impart PBM desirable electrical conductivity (up to 14,245 S m<sup>-1</sup>) and enhanced electrochemical performance. PBM composite film exhibits high specific capacitance (gravimetric capacitance of 550 F g<sup>-1</sup>, area capacitance of 879 mF cm<sup>-2</sup>) and excellent cycling stability (capacitance retention rate is 83.5% after 10,000 cycles) as freestanding supercapacitor electrode. Furthermore, the as-prepared symmetrical supercapacitor of sandwiched freestanding PBM papers shows high capacitance of 294 F g<sup>-1</sup>, desirable energy density (33.1 W h kg<sup>-1</sup> at power density of 243 W kg<sup>-1</sup>) and great capacitance retention at high current density. This facile strategy demonstrates a feasible approach for the fabrication of freestanding high-performance conductive polymer-based SCs electrode.

**Acknowledgments** This work was supported by the National Natural Science Foundation of China (Grant No. 51861165203, 51903166) and China Postdoctoral Science Foundation (2019M653398). We would like to thank the Analytical & Testing Centre of Sichuan University for XRD, SEM, TEM, FTIR and we would be grateful to Guiping Yuan for her help of TEM work.

## Compliance with ethical standards

**Conflict of interest** The authors declare that they have no conflict of interest.

## References

- Anasori B, Lukatskaya MR, Gogotsi Y (2017) 2D metal carbides and nitrides (MXenes) for energy storage. *Nat Rev Mater* 2:16098. <https://doi.org/10.1038/natrevmats.2016.98>
- Boota M, Gogotsi Y (2019) MXene—conducting polymer asymmetric pseudocapacitors. *Adv Energy Mater* 9:1802917. <https://doi.org/10.1002/aenm.201802917>
- Boota M, Hatzell KB, Kumbur EC, Gogotsi Y (2015) Towards high-energy-density pseudocapacitive flowable electrodes by the incorporation of hydroquinone. *Chemsuschem* 8:835–843. <https://doi.org/10.1002/cssc.201402985>
- Boota M, Anasori B, Voigt C et al (2016) Pseudocapacitive electrodes produced by oxidant-free polymerization of pyrrole between the layers of 2D titanium carbide (MXene). *Adv Mater* 28:1517–1522. <https://doi.org/10.1002/adma.201504705>
- Cao W-T, Chen F-F, Zhu Y-J et al (2018) Binary strengthening and toughening of MXene/cellulose nanofiber composite paper with nacre-inspired structure and superior electromagnetic interference shielding properties. *ACS Nano* 12:4583–4593. <https://doi.org/10.1021/acsnano.8b00997>
- Choi BG, Yang M, Hong WH et al (2012) 3D macroporous graphene frameworks for supercapacitors with high energy and power densities. *ACS Nano* 6:4020–4028. <https://doi.org/10.1021/nn3003345>
- Du X, Zhang Z, Liu W, Deng Y (2017) Nanocellulose-based conductive materials and their emerging applications in energy devices—a review. *Nano Energy* 35:299–320. <https://doi.org/10.1016/j.nanoen.2017.04.001>
- Edberg J, Inganäs O, Engquist I, Berggren M (2018) Boosting the capacity of all-organic paper supercapacitors using wood derivatives. *J Mater Chem A* 6:145–152. <https://doi.org/10.1039/C7TA06810G>
- El-Kady MF, Shao Y, Kaner RB (2016) Graphene for batteries, supercapacitors and beyond. *Nat Rev Mater* 1:16033. <https://doi.org/10.1038/natrevmats.2016.33>
- Ge H, Qi G, Kang E-T, Neoh KG (1994) Study of overoxidized polypyrrole using X-ray photoelectron spectroscopy. *Polymer* 35:504–508. [https://doi.org/10.1016/0032-3861\(94\)90503-7](https://doi.org/10.1016/0032-3861(94)90503-7)
- Ge D, Yang L, Fan L et al (2015) Foldable supercapacitors from triple networks of macroporous cellulose fibers, single-walled carbon nanotubes and polyaniline nanoribbons. *Nano Energy* 11:568–578. <https://doi.org/10.1016/j.nanoen.2014.11.023>
- Geng L, Zhu P, Wei Y et al (2019) A facile approach for coating Ti<sub>3</sub>C<sub>2</sub>T<sub>x</sub> on cotton fabric for electromagnetic wave shielding. *Cellulose* 26:2833–2847. <https://doi.org/10.1007/s10570-019-02284-5>
- Ghidiu M, Lukatskaya MR, Zhao M-Q et al (2014) Conductive two-dimensional titanium carbide ‘clay’ with high volumetric capacitance. *Nature* 516:78–81. <https://doi.org/10.1038/nature13970>
- He W, Zhao G, Sun P et al (2019) Construction of Longan-like hybrid structures by anchoring nickel hydroxide on yolk-shell polypyrrole for asymmetric supercapacitors. *Nano Energy* 56:207–215. <https://doi.org/10.1016/j.nanoen.2018.11.048>
- Heinze J, Frontana-Urbe BA, Ludwigs S (2010) Electrochemistry of conducting polymers—persistent models and new concepts. *Chem Rev* 110:4724–4771. <https://doi.org/10.1021/cr900226k>
- Huang Y, Li H, Wang Z et al (2016) Nanostructured polypyrrole as a flexible electrode material of supercapacitor. *Nano Energy* 22:422–438. <https://doi.org/10.1016/j.nanoen.2016.02.047>
- Jiang Q, Kurra N, Alhabeab M et al (2018) All pseudocapacitive MXene-RuO<sub>2</sub> asymmetric supercapacitors. *Adv Energy*

- Mater 8:1703043. <https://doi.org/10.1002/aenm.201703043>
- Jin X, Wang J, Dai L et al (2020) Flame-retardant poly(vinyl alcohol)/MXene multilayered films with outstanding electromagnetic interference shielding and thermal conductive performances. *Chem Eng J* 380:122475. <https://doi.org/10.1016/j.cej.2019.122475>
- Kashani H, Chen L, Ito Y et al (2016) Bicontinuous nanotubular graphene–polypyrrole hybrid for high performance flexible supercapacitors. *Nano Energy* 19:391–400. <https://doi.org/10.1016/j.nanoen.2015.11.029>
- Ke Q, Guan C, Zhang X et al (2017) Surface-charge-mediated formation of H-TiO<sub>2</sub>/Ni(OH)<sub>2</sub> heterostructures for high-performance supercapacitors. *Adv Mater* 29:1604164. <https://doi.org/10.1002/adma.201604164>
- Lei J-C, Zhang X, Zhou Z (2015) Recent advances in MXene: preparation, properties, and applications. *Front Phys* 10:276–286. <https://doi.org/10.1007/s11467-015-0493-x>
- Li S-C, Hu B-C, Ding Y-W et al (2018) Wood-derived ultrathin carbon nanofiber aerogels. *Angew Chem Int Ed* 57:7085–7090. <https://doi.org/10.1002/anie.201802753>
- Liu T, Finn L, Yu M et al (2014) Polyaniline and polypyrrole pseudocapacitor electrodes with excellent cycling stability. *Nano Lett* 14:2522–2527. <https://doi.org/10.1021/nl500255v>
- Liu Y, Zhou J, Tang J, Tang W (2015) Three-dimensional, chemically bonded polypyrrole/bacterial cellulose/graphene composites for high-performance supercapacitors. *Chem Mater* 27:7034–7041. <https://doi.org/10.1021/acs.chemmater.5b03060>
- Liu J, Liu Z, Zhang H-B et al (2020) Ultrastrong and highly conductive MXene-based films for high-performance electromagnetic interference shielding. *Adv Elect Mater* 6:1901094. <https://doi.org/10.1002/aelm.201901094>
- Lota K, Khomenko V, Frackowiak E (2004) Capacitance properties of poly(3,4-ethylenedioxythiophene)/carbon nanotubes composites. *J Phys Chem Solids* 65:295–301. <https://doi.org/10.1016/j.jpcs.2003.10.051>
- Lukatskaya MR, Mashtalir O, Ren CE et al (2013) Cation intercalation and high volumetric capacitance of two-dimensional titanium carbide. *Science* 341:1502–1505. <https://doi.org/10.1126/science.1241488>
- Lukatskaya MR, Kota S, Lin Z et al (2017) Ultra-high-rate pseudocapacitive energy storage in two-dimensional transition metal carbides. *Nat Energy* 2:17105. <https://doi.org/10.1038/nenergy.2017.105>
- Ma L, Liu R, Niu H et al (2016a) Freestanding conductive film based on polypyrrole/bacterial cellulose/graphene paper for flexible supercapacitor: large areal mass exhibits excellent areal capacitance. *Electrochim Acta* 222:429–437. <https://doi.org/10.1016/j.electacta.2016.10.195>
- Ma L, Liu R, Niu H et al (2016b) Flexible and freestanding supercapacitor electrodes based on nitrogen-doped carbon networks/graphene/bacterial cellulose with ultrahigh areal capacitance. *ACS Appl Mater Interfaces* 8:33608–33618. <https://doi.org/10.1021/acsami.6b11034>
- Mu X, Wang D, Du F et al (2019) Revealing the pseudo-intercalation charge storage mechanism of mxenes in acidic electrolyte. *Adv Funct Mater*. <https://doi.org/10.1002/adfm.201902953>
- Naguib M, Mochalin V, Barsoum M et al (2014) 25th Anniversary article: MXenes: a new family of two-dimensional materials. *Adv Mater* 26:992–1005. <https://doi.org/10.1002/adma.201304138>
- Qiu Y, Qiu L, Cui J, Wei Q (2016) Bacterial cellulose and bacterial cellulose-vaccarin membranes for wound healing. *Mater Sci Eng C* 59:303–309. <https://doi.org/10.1016/j.msec.2015.10.016>
- Simon P, Gogotsi Y (2008) Materials for electrochemical capacitors. *Nat Mater* 7:845–854. <https://doi.org/10.1038/nmat2297>
- Snook GA, Kao P, Best AS (2011) Conducting-polymer-based supercapacitor devices and electrodes. *J Power Sour* 196:1–12. <https://doi.org/10.1016/j.jpowsour.2010.06.084>
- Song Y, Xu J-L, Liu X-X (2014) Electrochemical anchoring of dual doping polypyrrole on graphene sheets partially exfoliated from graphite foil for high-performance supercapacitor electrode. *J Power Sour* 249:48–58. <https://doi.org/10.1016/j.jpowsour.2013.10.102>
- Song Y, Liu T-Y, Xu X-X et al (2015) Pushing the cycling stability limit of polypyrrole for supercapacitors. *Adv Funct Mater* 25:4626–4632. <https://doi.org/10.1002/adfm.201501709>
- VahidMohammadi A, Moncada J, Chen H et al (2018) Thick and freestanding MXene/PANI pseudocapacitive electrodes with ultrahigh specific capacitance. *J Mater Chem A* 6:22123–22133. <https://doi.org/10.1039/C8TA05807E>
- Wan C, Jiao Y, Li J (2017) Flexible, highly conductive, and freestanding reduced graphene oxide/polypyrrole/cellulose hybrid papers for supercapacitor electrodes. *J Mater Chem A* 5:3819–3831. <https://doi.org/10.1039/C6TA04844G>
- Wang G, Zhang L, Zhang J (2012) A review of electrode materials for electrochemical supercapacitors. *Chem Soc Rev* 41:797–828. <https://doi.org/10.1039/C1CS15060J>
- Wang H, Bian L, Zhou P et al (2013) Core–sheath structured bacterial cellulose/polypyrrole nanocomposites with excellent conductivity as supercapacitors. *J Mater Chem A* 1:578–584. <https://doi.org/10.1039/C2TA00040G>
- Wang Y, Lin X, Liu T et al (2018) Wood-derived hierarchically porous electrodes for high-performance all-solid-state supercapacitors. *Adv Funct Mater* 28:1806207. <https://doi.org/10.1002/adfm.201806207>
- Wu Z-Y, Liang H-W, Chen L-F et al (2016) Bacterial cellulose: a robust platform for design of three dimensional carbon-based functional nanomaterials. *Acc Chem Res* 49:96–105. <https://doi.org/10.1021/acs.accounts.5b00380>
- Xiong D, Li X, Bai Z, Lu S (2018) Recent advances in layered Ti<sub>3</sub>C<sub>2</sub>T<sub>x</sub> MXene for electrochemical energy storage. *Small* 14:1703419. <https://doi.org/10.1002/sml.201703419>
- Xu J, Zhu L, Bai Z et al (2013) Conductive polypyrrole–bacterial cellulose nanocomposite membranes as flexible supercapacitor electrode. *Org Electron* 14:3331–3338. <https://doi.org/10.1016/j.orgel.2013.09.042>
- Zhang LL, Zhao XS (2009) Carbon-based materials as supercapacitor electrodes. *Chem Soc Rev* 38:2520–2531. <https://doi.org/10.1039/B813846J>
- Zhang Z, Xiao F, Qian L et al (2014) Facile synthesis of 3D MnO<sub>2</sub>–graphene and carbon nanotube–graphene composite networks for high-performance, flexible, all-solid-state asymmetric supercapacitors. *Adv Energy Mater* 4:1400064. <https://doi.org/10.1002/aenm.201400064>

- Zhang Z, Li L, Qing Y et al (2019) Manipulation of nanoplate structures in carbonized cellulose nanofibril aerogel for high-performance supercapacitor. *J Phys Chem C* 123: 23374–23381. <https://doi.org/10.1021/acs.jpcc.9b06058>
- Zhao D, Zhu Y, Cheng W et al (2020) Cellulose-based flexible functional materials for emerging intelligent electronics. *Adv Mater*. <https://doi.org/10.1002/adma.202000619>
- Zhu M, Huang Y, Deng Q et al (2016) Highly flexible, free-standing supercapacitor electrode with enhanced performance obtained by hybridizing polypyrrole chains with MXene. *Adv Energy Mater* 6:1600969. <https://doi.org/10.1002/aenm.201600969>
- Zhu S, Li L, Liu J et al (2018) Structural directed growth of ultrathin parallel birnessite on  $\beta$ -MnO<sub>2</sub> for high-performance asymmetric supercapacitors. *ACS Nano* 12:1033–1042. <https://doi.org/10.1021/acsnano.7b03431>

**Publisher's Note** Springer Nature remains neutral with regard to jurisdictional claims in published maps and institutional affiliations.